The Astrophysical Journal, 782:10 (14pp), 2014 February 10 doi:10.1088/0004-637X/782/1/10

ANALYSIS OF MOLECULAR HYDROGEN ABSORPTION TOWARD QSO B0642−5038 FOR A VARYING PROTON-TO-ELECTRON MASS RATIO*

J. Bagdonaite[1], W. Ubachs[1], M. T. Murphy[2], and J. B. Whitmore[2]
[1] Department of Physics and Astronomy, VU University Amsterdam, De Boelelaan 1081, 1081-HV Amsterdam, The Netherlands; j.bagdonaite@vu.nl
[2] Centre for Astrophysics and Supercomputing, Swinburne University of Technology, Victoria 3122, Australia
Received 2013 August 5; accepted 2013 December 10; published 2014 January 21

ABSTRACT

Rovibronic molecular hydrogen (H_2) transitions at redshift $z_{abs} \simeq 2.659$ toward the background quasar B0642−5038 are examined for a possible cosmological variation in the proton-to-electron mass ratio μ. We utilize an archival spectrum from the Very Large Telescope/Ultraviolet and Visual Echelle Spectrograph (UVES) with a signal-to-noise ratio of ∼35 per 2.5 km s^{-1} pixel at the observed H_2 wavelengths (335–410 nm). Some 111 H_2 transitions in the Lyman and Werner bands have been identified in the damped Lyα system for which a kinetic gas temperature of ∼84 K and a molecular fraction $\log f = -2.18 \pm 0.08$ are determined. The H_2 absorption lines are included in a comprehensive fitting method, which allows us to extract a constraint on a variation of the proton–electron mass ratio $\Delta\mu/\mu$ from all transitions at once. We obtain $\Delta\mu/\mu = (17.1 \pm 4.5_{stat} \pm 3.7_{sys}) \times 10^{-6}$. However, we find evidence that this measurement has been affected by wavelength miscalibration errors recently identified in UVES. A correction based on observations of objects with solar-like spectra gives a smaller $\Delta\mu/\mu$ value and contributes to a larger systematic uncertainty: $\Delta\mu/\mu = (12.7 \pm 4.5_{stat} \pm 4.2_{sys}) \times 10^{-6}$.

Key words: galaxies: high-redshift – ISM: molecules – quasars: absorption lines

Online-only material: color figures

1. INTRODUCTION

The fact that only 4% of the energy density content in the universe can be explained within the current framework of particle physics suggests that the standard model is incomplete. In this context, observational attempts to detect variation of fundamental constants serve as one of the guiding tools for theoretical extensions in both cosmology and the standard model. For instance, the theories that intend to unify gravitation with the other three fundamental forces by introducing additional spatial dimensions accommodate cosmologically varying constants quite naturally (Uzan 2011). Alternatively, additional quantum fields such as the dilaton field may be invoked, predicting scenarios of varying constants complying with conservation of energy (Bekenstein 2002). Experimental methods are established for probing dimensionless constants such as the fine structure constant $\alpha \equiv e^2/(4\pi\epsilon_0\hbar c)$, which sets the quantum electrodynamical scale, and the proton-to-electron mass ratio $\mu \equiv m_p/m_e$, which is sensitive to the ratio of the chromodynamic scale to the electroweak scale (Flambaum et al. 2004).

The redshifted spectra of quasars contain multiple absorption lines arising from cold gas along the line of sight to Earth. These absorption lines serve as a means to probe the high-redshift universe, also making it possible to study varying fundamental constants. In the case of varying μ and α, the absorbers that have the highest neutral hydrogen column densities, known as the damped Lyα (DLA) systems, are of particular interest since they are most likely to contain molecular and atomic species that have μ- or α-sensitive energy levels. If μ or α changes with redshift, the relative pattern of the transitions, which is known to a very high accuracy from laboratory experiments, is altered in a specific and calculable manner, different from the overall redshift.

A variation of μ can be detected through the Lyman and Werner bands of molecular hydrogen (H_2; $\lambda_{rest} < 1150$ Å), which are observable from ground-based observatories if absorption occurs at redshifts $z_{abs} > 2$ (Thompson 1975). The proton-to-electron mass ratio at high redshift μ_z is measured as a shift with respect to the present-day value μ_0: $\Delta\mu/\mu = (\mu_z - \mu_0)/\mu_0$. H_2 absorption is detected quite rarely, so far in some 20 DLAs, only a few of which are suitable for high-accuracy μ analysis, i.e., providing $\Delta\mu/\mu$ constraints at a level of $<10^{-5}$ (Ubachs et al. 2011). For comparison, the atomic species (Mg, Fe, Cr, Zn, etc.) sensitive to a variation of α have been detected in some 300 absorption systems, which has allowed the constant to be mapped over a broad spatial and temporal range and has yielded an indication of spatial variation (King et al. 2012). As for μ, the H_2 absorbing systems toward Q0347−383 at $z_{abs} = 3.02$, Q0405−443 at $z_{abs} = 2.59$, Q0528−250 at $z_{abs} = 2.81$, J2123−005 at $z_{abs} = 2.06$, Q2348−011 at $z_{abs} = 2.42$, and HE0027−1836 at $z_{abs} = 2.40$ have been analyzed thus far at high accuracy (King et al. 2008, 2011; Malec et al. 2010a; van Weerdenburg et al. 2011; Wendt & Molaro 2012; Bagdonaite et al. 2012; Rahmani et al. 2013). As a result of improving data quality and discussions on appropriate analysis methods, most of the absorbers have been studied more than once, sometimes leading to controversial outcomes. For example, the study by Ivanchik et al. (2005) on Q0347−383 and Q0405−443 yielded an indication of μ variation based on a laboratory-based H_2 absorption spectrum using classical spectroscopy. An updated extreme ultraviolet laser spectrum of H_2 by Reinhold et al. (2006) provided extended evidence for such a possible variation of μ. However, a reanalysis of the astrophysical spectra of Q0347−383 and Q0405−443 by King et al. (2008), using the so-called comprehensive fitting analysis also adopted in the present study, lowered the significance of the effect to a $<2\sigma$ deviation: $\Delta\mu/\mu = (8.2 \pm 7.4) \times 10^{-6}$ and $(10.1 \pm 6.2) \times 10^{-6}$ in the two sightlines, respectively.

* Based on data obtained with Ultraviolet and Visual Echelle Spectrograph (UVES) at the Very Large Telescope of the European Southern Observatory.

In contrast, observations of J2123−005 with Keck/High Resolution Echelle Spectrometer (HIRES) delivered a μ constraint (Malec et al. 2010a) that was later reproduced by an independent revision (but the same spectral analysis method) using a Very Large Telescope (VLT)/Ultraviolet and Visual Echelle Spectrograph (UVES) spectrum of the same object (van Weerdenburg et al. 2011). Altogether, the H_2 studies converge in a constraint on the variation of μ at the level of $\Delta\mu/\mu < 1 \times 10^{-5}$ in the redshift range $z = 2$–3. Given the sensitivity coefficients of H_2 ranging from −0.02 to +0.05, a substantially higher accuracy in $\Delta\mu/\mu$ can only be achieved by drastically improving the quality (signal-to-noise ratio (S/N)) of the spectra or by increasing the number of absorbers. The same holds true for the other two weak shifters: HD and CO molecules (Ivanov et al. 2008; Salumbides et al. 2012).

As an alternative to H_2, inversion transitions of ammonia and rotational transitions of methanol can be used for they are, respectively, two or three orders of magnitude more sensitive to μ variation compared to H_2 (Flambaum & Kozlov 2007; Jansen et al. 2011; Levshakov et al. 2011). Detections of ammonia at redshifts $z_{\rm abs} = 0.89$ and 0.69 are known currently, yielding 1σ constraints on μ at the level of $(1.0 \pm 4.7) \times 10^{-7}$ and $(-3.5 \pm 1.2) \times 10^{-7}$ (Henkel et al. 2009; Kanekar 2011). Further observations of the object at redshift $z_{\rm abs} = 0.89$, a lensing galaxy toward the quasar PKS1830−211, has yielded a detection of methanol resulting in a stringent constraint of $\Delta\mu/\mu = (0.0 \pm 1.0) \times 10^{-7}$ (Bagdonaite et al. 2013b). Although ammonia and methanol are more favorable probes because of the high sensitivity, their detections are extremely rare. Thus, molecular hydrogen remains a target molecule for μ variation studies, especially at high redshifts where no constraints from ammonia or methanol are available yet.

In the study presented here, molecular hydrogen transitions at redshift $z_{\rm abs} = 2.659$ toward the background quasar B0642−5038 are analyzed in the search for a cosmological variation in the proton-to-electron mass ratio μ.

2. METHOD

2.1. Molecular Hydrogen

For the ith transition of H_2 detected in a cloud at redshift $z_{\rm abs}$, the observed wavelength is expressed as

$$\lambda_i = \lambda_i^0 (1 + z_{\rm abs}) \left(1 + K_i \frac{\Delta\mu}{\mu}\right), \quad (1)$$

where λ_i^0 is the rest wavelength of the transition and K_i is a sensitivity coefficient of the transition, which expresses its shifting power and direction due to varying μ. As for H_2 transitions, we employ sensitivity coefficients K_i defined as

$$K_i = \frac{\mu}{\lambda_i} \frac{d\lambda_i}{d\mu}. \quad (2)$$

Note that this definition yields a different sign than usually adopted for the transitions in the radio domain, where a relation is defined in terms of frequency: $\Delta\nu/\nu = K_i \Delta\mu/\mu$. Nevertheless, the sign of $\Delta\mu/\mu$ remains unaffected; that is, direct comparison of the optical and radio constraints is possible. From Equation (1) it follows that from two transitions of different sensitivities, one can determine both the redshift and $\Delta\mu/\mu$. In practice, it is desirable to use as many H_2 transitions as possible since the cumulative signal from multiple

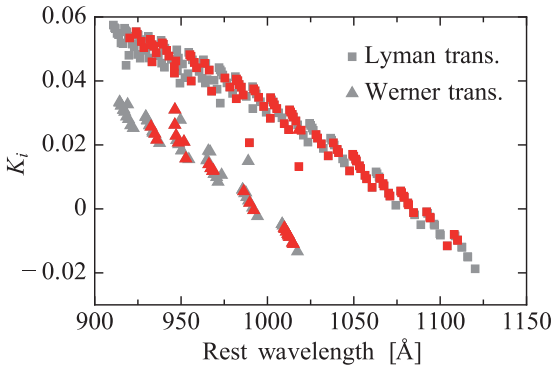

Figure 1. Sensitivity coefficients K_i of the Lyman and Werner transitions of H_2 plotted against the rest wavelength. The transitions that were suitable for the $\Delta\mu/\mu$ analysis are marked in red.

(A color version of this figure is available in the online journal.)

transitions is necessary to balance relatively small sensitivity coefficients. Compared to the uncertainties of line positions in the quasar spectrum, the laboratory wavelengths of H_2 at accuracies $\Delta\lambda/\lambda \sim 5 \times 10^{-8}$ can be considered to be exact for our purpose (Salumbides et al. 2011). The K_i coefficients of H_2 have been calculated within a semiempirical framework (Ubachs et al. 2007, used in the present analysis), including effects beyond the Born–Oppenheimer approximation, and from ab initio methods (Meshkov et al. 2006). The K_i values from these two approaches are in agreement within 1%. A comprehensive list of laboratory wavelengths, K_i coefficients, oscillator strengths, and damping parameters of H_2/HD transitions is provided by Malec et al. (2010b) and implemented in this work (also see Figure 1).

2.2. Fitting Method

In this study we employ a fitting technique that relies on a number of physical assumptions allowing for simultaneous modeling of all H_2 transitions and nearby H I lines at once. This method is known as the "comprehensive fitting method" to distinguish it from a "line-by-line" method, in which, as its name suggests, each transition is fitted independently of the others. The former technique allows us to include more transitions than the latter, as the fitting of the surrounding Lyα forest is readily possible. Also, the line-by-line method may not be applicable for the H_2 absorbers with complex profiles (multiple H_2 clouds distributed close to each other in the velocity space). A more detailed comparison of these two fitting approaches is outlined by King et al. (2008) and Malec et al. (2010a).

In short, the analysis of H_2 absorption spectra can be described as a three-step process: (1) selection of potentially usable transitions, (2) setting up and refining the fit, and (3) μ derivation and testing.

The analysis starts from visual inspection of the spectrum. The goal is to compose a list of spectral segments each containing an H_2 line and some surrounding buffer region so that any overlapping non-H_2 feature can be modeled too. Quite frequently, two or more adjacent H_2 lines are included in a single region when they are too close to be fitted separately. Being distributed over the Lyα forest, most of the H_2 transitions unavoidably overlap with H I lines. In some cases a strongly saturated H I absorption may render overlapping H_2 lines useless, in which case they are neglected. Additionally, some H_2 transitions can be excluded because of an overlap with narrow metal or unidentified lines if these are unconstrainable (see Section 4.2). The

number of selected H_2 lines is usually in the range between 40 and 100.

Once the list is complete, the nonlinear least-squares Voigt profile fitting program VPFIT 9.5[3] is used to model the absorption lines. A Voigt profile represents an absorption line that is broadened by Doppler and Lorentzian mechanisms and convolved with an instrumental profile (assumed to be Gaussian). The Doppler broadening is caused by the thermal (or large-scale turbulent) motion of the molecules/atoms, while the Lorentzian broadening is due to the finite lifetimes of the excited states. All H_2 and surrounding neutral hydrogen lines are modeled simultaneously. For each transition, a Voigt profile is assigned by providing three adjustable parameters: the redshift of the transition z, the column density N, and the velocity width b. Initial user-supplied parameter guesses for the considered lines are fed to VPFIT, which finds the best match between the model and data by minimizing the goodness-of-fit parameter χ^2. At each iteration, VPFIT checks the change in the relative χ^2 and reports convergence once an improvement tolerance is met. The stopping criterion, the stepping size for each of the free parameters, and their limits are user defined. Further, the model is refined manually by adding or removing lines (i.e., H_2, H I Lyα, and/or metallic ion transitions) and again fitted with VPFIT. This process is repeated until a statistically acceptable fit is achieved. There are several main guidelines for a statistically acceptable model.

1. The residuals of each fitted region should be well behaved, that is, they should be free from nonrandom trends. This is verified by inspecting each individual region by eye and by constructing a composite residual spectrum (CRS), which is an even more sensitive tool for systematic fitting problems. To compose a CRS, we select the cleanest H_2 transitions, normalize their residuals (fit minus data) by the flux error, and shift them to a common redshift/velocity scale, where they are averaged together. If any systematic underfitting is present, it becomes "amplified" in the CRS.
2. A statistically adequate fit should have a χ^2 per degree of freedom χ^2_ν around 1. For the entire fit with ν degrees of freedom,[4] a χ^2/ν is reported by VPFIT. Competing models can be rated according to their relative values of χ^2_ν.
3. The statistically most adequate model has the lowest Akaike information criterion (for finite sample sizes abbreviated AICC; Akaike 1974). The AICC is a method to approve or disapprove the addition of absorption lines (or, more often in our case, velocity components (VCs) of H_2). It is defined as

$$\mathrm{AICC} = \chi^2 + 2p + \frac{2p(p+1)}{n-p-1}, \quad (3)$$

where n is the number of data points fitted and p is the number of free parameters. When comparing two models, the model with a lower AICC is statistically preferred. More precisely, $\Delta\mathrm{AICC} > 5$ is considered strong evidence and $\Delta\mathrm{AICC} > 10$ is considered very strong evidence for choosing the model with a lower AICC.

[3] Developed by B. Carswell et al.; http://www.ast.cam.ac.uk/~rfc/vpfit.html. We use an upgraded version of VPFIT 9.5 in which the Gauss–Newton optimization algorithm is augmented with the Levenberg–Marquardt algorithm, and computing can be done in parallel on multiple cores. These changes were implemented by J. King (UNSW).

[4] The degrees of freedom in VPFIT are assumed to be $\nu = n - p$, where n is the number of data points fitted and p is the number of free parameters. However, ν is not defined in such way for a nonlinear model. The rationale for this assumption was discussed by King (2012).

The number of so-called VCs is an important ingredient in deciding which model is the best to represent a H_2 spectrum. The light coming from a quasar can be absorbed by multiple H_2 clouds in the DLA (or a single cloud can contain clumps with varying density, turbulence, and temperature), resulting in multiple spectral features for every H_2 transition. At first, the number of VCs is estimated by eye. Then, once the initial model is fitted with VPFIT, more H_2 components might be added if the residuals show any hints of underfitting. VPFIT rejects the added components if data do not support them. As explained above, the necessity to include more components is also assessed from the behavior of χ^2_ν and AICC and the residuals: if these parameters improve, the model is considered more adequate. One should be careful not to underfit: it has been shown that underfitting is more prone to cause biases in the $\Delta\mu/\mu$ or $\Delta\alpha/\alpha$ constraints than overfitting (Murphy et al. 2008a, 2008b).

As mentioned before, each Voigt profile is described by three free parameters. By employing the comprehensive fitting method, we tie the free parameters among different transitions. For a single VC of H_2 the following physical restrictions are imposed: (1) the same column density for all transitions from a single J level, (2) the same z parameter for all transitions, and (3) the same turbulent b parameter for all transitions. Some assumptions can be released if a reasonable fit cannot be achieved, but as a rule, we aim to base our fit as much as possible on molecular physics information on the H_2 molecule. Besides the free parameters, a Voigt profile for each transition involves three fixed parameters that are obtained from the molecular physics: rest wavelength λ_i, oscillator strength I_i, and damping parameter Γ_i.

Once the model is optimized, the last free parameter, $\Delta\mu/\mu$, is introduced. A single $\Delta\mu/\mu$ parameter allows relative shifting of the H_2 transitions in accordance with Equation (1). It is important to introduce this fourth parameter only after the model is finalized because, otherwise, it can acquire a false value to accommodate imperfections of the fit. The very last step is to test how sensitive the derived $\Delta\mu/\mu$ constraint is to the physical assumptions and fitting choices made. These tests can include μ constraints derived from various data cuts: separate J levels, separate Werner transitions and Lyman transitions, regions with no overlapping metal lines, a fit with no assumption about b in different J levels, etc.

3. DATA

The spectrum of QSO B0642−5038 (R.A. $06^h43^m27\overset{s}{.}0024$, decl. $-50°41'12\overset{''}{.}804$, J2000, visible magnitude $V = 18.5$) was obtained on VLT/UVES under three different programs (their IDs along with the observational settings are listed in Table 1). A concise report on the observations was given by Noterdaeme et al. (2008). All raw science and calibration data were retrieved from the publicly available European Southern Observatory (ESO) archive.[5] The total exposure time of the selected data makes up 22.4 hr. The combined spectrum covers wavelengths from 330 to 1040 nm with two gaps due to separation between the CCDs at 452.1–461.9 and 842.5–856.9 nm. The ratio of average seeing to slit width is 1.1. More than half of the exposures were followed immediately by ThAr calibration (so-called attached ThAr calibration), thereby minimizing the possibility that the optical system can be disturbed by the grating reset. Most of the science frames were obtained with a slit

[5] The ESO archive is accessible via http://archive.eso.org/eso/eso_archive_main.html.

Table 1
ESO Archival Data of the B0642−5038 and Ceres Observations with VLT/UVES

Program ID	Obs. Date	Blue/Red (nm)	Slit (arcsec)	Integration Time (s)	Seeing (arcsec)	ThAr Calibration
B0642−5038						
073.A-0071(A)	2004 Sep 17	390/580	1.2	5500	1.89	Nonatt.
	2004 Sep 18	390/580	1.2	6000	1.90	Nonatt.
	2004 Sep 19	390/580	0.8	6000	1.00	Nonatt.
074.A-0201(A)	2004 Oct 9	390/850	0.8	5800	0.60	Nonatt.
	2004 Oct 10	390/850	0.8	5500	0.37	Nonatt.
080.A-0288(A)	2007 Dec 11	390/564	1.0	3725	1.00	Att.
	2008 Jan 3	390/564	1.0	3725	0.91	Att.
	2008 Jan 4	390/564	1.0	3725	1.77	Att.
	2008 Jan 4	390/564	1.0	3725	1.66	Att.
	2008 Jan 4	390/564	1.0	1389	1.69	Att.
	2008 Jan 6	390/564	1.0	2104	1.24	Att.
	2008 Jan 6	390/564	1.0	3725	1.24	Att.
	2008 Jan 6	390/564	1.0	3725	1.08	Att.
	2008 Jan 7	390/564	1.0	3725	0.84	Att.
	2008 Jan 13	390/564	1.0	3725	1.00	Att.
	2008 Jan 16	390/564	1.0	3725	0.85	Att.
	2008 Feb 6	390/564	1.0	3725	0.82	Att.
	2008 Feb 7	390/564	1.0	3725	0.90	Att.
	2008 Feb 9	390/564	1.0	3725	0.80	Att.
	2008 Feb 10	390/564	1.0	3725	0.81	Att.
Ceres						
080.C-0881(B)	2007 Dec 5	346	1.0	2850	1.32	Nonatt.
HD 28099						
380.C-0773(A)	2008 Jan 11	390/564	0.7	264	1.27	Nonatt.
	2008 Jan 11	390/564	0.7	264	1.21	Nonatt.
HD 76151						
380.C-0773(A)	2008 Jan 11	390/564	0.7	67	0.69	Att.

Notes. The total combined integration time on the B0642−5038 makes up 22.4 hr in each arm, 14.4 hr of which have the attached ThAr calibration. The CCD binning mode was 2 × 2 for all B0642−5038 frames. Air masses were in the range between 1.113 and 1.562. For Ceres, HD 28099, and HD 76151 the binning mode was 1 × 1.

width of 1.″0, which with 2 × 2 on-chip binning translates to an instrumental velocity resolution of $\sigma_v \simeq 3.1$ km s^{-1} in the blue part and ≃3.3 km s^{-1} in the red part (resolving powers $R \sim 41{,}000$ and 39,000, respectively). However, the target is a point source, and unlike the calibration lamp, which illuminates the entire slit, it only covers the central part of the slit; thus, a better resolution is expected. Here, we adopt a resolution of $\sigma_v \simeq 2.9$ km s^{-1}, which is ∼6% better than the formally derived value.

We used the ESO UVES Common Pipeline Language software suite to optimally extract and calibrate the echelle orders and an open-source, publicly available, custom program UVES_POPLER[6] to combine multiple exposures into a single, one-dimensional (1D), normalized spectrum on a vacuum-heliocentric wavelength scale. The Pipeline first bias corrects and flat fields the quasar exposures. It then constrains a physical model of where the quasar light is expected to fall on the CCDs with the aid of quartz and ThAr exposures taken through a "pinhole" instead of a standard slit. The quasar light is then separated from the background and extracted using an optimal extraction method. The ThAr flux (from the calibration frame taken with the same slit as the quasar) was extracted with the same optimal weights derived from the corresponding quasar exposure. The selection of ThAr lines and the establishment of a wavelength solution followed the method described in Murphy et al. (2007). UVES_POPLER takes the pixel-space flux spectra from each order of each exposure and disperses all of them onto a common loglinear wavelength scale with a dispersion bin of 2.5 km s^{-1}. Before redispersion, the wavelength solution for each exposure (established from its corresponding ThAr calibration frame) was corrected from air to vacuum using the Edlén (1966) formula and placed in the heliocentric reference frame using the time of the midpoint of the exposure's integration as a reference. The method of combining the exposures is based on the relative flux scaling between all available overlapping orders weighted by their inverse variance. When combining these scaled orders in this weighted fashion, UVES_POPLER applies an automated algorithm for cosmic ray rejection while other spectral artifacts are inspected and removed manually. The continuum is fitted manually with low-order polynomials. Small constant or linear local changes of the continuum and corrections to zero level are permitted in later stages of the analysis.

4. ANALYSIS

4.1. Damped Lyα System in the QSO B0642−5038 Spectrum

The quasar is located at redshift $z = 3.09$, thereby defining the extent of the Lyα forest. The quasar radiation is cut off at the

[6] http://astronomy.swin.edu.au/∼mmurphy/UVES_popler

Table 2
A List of the H_2 Transitions Used in the Present Study

J Level	Lyman Transitions	Werner Transitions	n_{trans}
$J = 0$	L0R0, L1R0, L2R0, L4R0, L7R0, L8R0, L14R0, L17R0	W3R0	9
$J = 1$	L0P1, L1P1, L2P1, L2R1, L4P1, L4R1, L5P1, L7P1, L7R1, L8P1, L9P1, L9R1, L10P1, L10R1, L12R1, L13P1, L13R1, L14R1, L15P1, L15R1, L16P1, L17R1,	W0Q1, W2Q1, W3R1	25
$J = 2$	L0R2, L1R2, L2P2, L2R2, L3P2, L3R2, L4P2, L4R2, L5P2, L6P2, L7P2, L7R2, L8P2, L8R2, L9P2, L10P2, L10R2, L11P2, L12P2, L13P2, L15P2, L16P2, L16R2, L17P2, L18P2	W0Q2, W0P2, W1R2, W2Q2, W2P2, W4P2, W3R2	32
$J = 3$	L2R3, L2P3, L3P3, L3R3, L4P3, L4R3, L5R3, L6P3, L6R3, L7P3, L9P3, L10R3, L11P3, L12R3, L13R3, L15R3, L16R3, L17R3	W0R3, W0Q3, W0P3, W1Q3, W3R3, W3P3, W4P3	25
$J = 4$	L1P4, L3R4, L4P4, L4R4, L5P4, L6P4, L8P4, L8R4, L9P4, L10R4, L11P4, L14P4, L15R4, L17P4	W0Q4, W0R4, W1Q4, W2R4, W3Q4, W4Q4	20
Total			111

Note. The underlined transitions are overlapped by narrow lines of known or unknown origin, and the corresponding regions are excluded in one of the tests.

shortest recorded wavelengths since a DLA at redshift $z = 2.659$ produces the Lyman break at <335 nm. The H_2 lines associated with the DLA are spread in the range from 335 to 410 nm. The S/N of the continuum at the center of this range (∼370 nm) is 35 per 2.5 km s^{-1} pixel. The column density of the neutral hydrogen contained by the DLA is $\log N = 20.95 \pm 0.08$ cm^{-2} (Noterdaeme et al. 2008).

4.2. Creating and Selecting the Most Adequate Absorption Model

We detect molecular hydrogen transitions up to rotational levels with $J = 4$. In total there are ∼250 potentially useful Lyman and Werner transitions from $J \leqslant 4$ and vibrational levels $v \leqslant 18$ (Lyman) and $v \leqslant 5$ (Werner). We select those H_2 transitions that are neither overlapped by saturated H I nor too weak, as suitable for the analysis. Altogether, 72 regions have been selected, containing a total of 111 H_2 transitions (see Table 2; Figure 2 displays a part of the spectrum with selected transitions). Each of the H_2 regions is inspected for possible intervening metal lines. The redshifts of absorbing systems with metals in this sightline are determined by identifying the lines in the spectrum redward from the Lyα emission of the quasar. Some C IV systems could be found blueward too. All of them are listed in Table 3. We identify seven H_2 transitions that are overlapped by metal lines and several more that are situated next to some narrow unidentified lines. To constrain the relevant metal transitions, three more regions containing their counterparts in the red part of the spectrum are added to the region sample. For instance, the H_2 transitions L2P(2) and L2R(3), redshifted to 3954–3958 Å, are overlapping with an Fe II transition ($\lambda_{rest} = 1081.87$ Å) of the DLA. To constrain the absorption of Fe II, we use a different Fe II transition that is outside the Lyα forest ($\lambda_{rest} = 1608.45$ Å).

Although the H_2 absorption is seen in a single feature upon first inspection (see Figure 3), the possibility of a more complex underlying structure is explored (see Section 2.2 for motivation for doing so). A second VC is added near the first VC, and fitting is performed with VPFIT. Several fits with various combinations of the initial values for z, b, and N of the two components have been carried out to ensure robustness of such a model. For each VC, the free parameters are connected to each other as described in Section 2.2. We find that the model with two VCs (2VC) is statistically more preferable than the model with one VC (1VC): it has a χ^2_ν of 1.189 and an AICC of 10165.6, compared to, respectively, 1.193 and 10190.4 for the 1VC model. However, the additional VC, present in the $J = 0$ and 1 transitions only, is very weak (a column density of some four orders of magnitude lower than the main component is found), and its position has a very large uncertainty (see Table 4) that later translates to a minor increase in the uncertainty of $\Delta\mu/\mu$. The CRS of the 1VC model does not show any significant underfitting (see Figure 4). Attempts to compose a stable 3VC model were unsuccessful. Thus, on the basis of the statistical parameters, we adopt the 2VC

Table 3
Metal Absorbers in the Line of Sight Toward the B0642−5038

Redshift	Species
1.545[a], 1.647, 1.691, 1.852, 1.987, 2.031, 2.126, 2.204, 2.348, 2.423, 2.500, 2.912	C IV
1.561	C I, C IV
2.029	C IV, Si IV, Si III
2.082	C IV, Si IV, Si III
2.510	C IV, N V, Si IV, O VI
2.521	C IV, Al II
2.659[b]	C IV, C II, Al III, Si II[a], Si III, Si IV, P II, Cr II, Ni II, Zn II, Al II, Fe II[a], N I, O I, C I, C III, C II*
2.899	C IV[a], C III[a], N V, Si IV, Si III, S IV, O VI
2.955	C IV, C III, O VI
2.967	C IV, O VI

Notes.
[a] Metal absorptions overlapping H_2 (or those used to constrain them).
[b] The DLA system currently analyzed for μ variation.

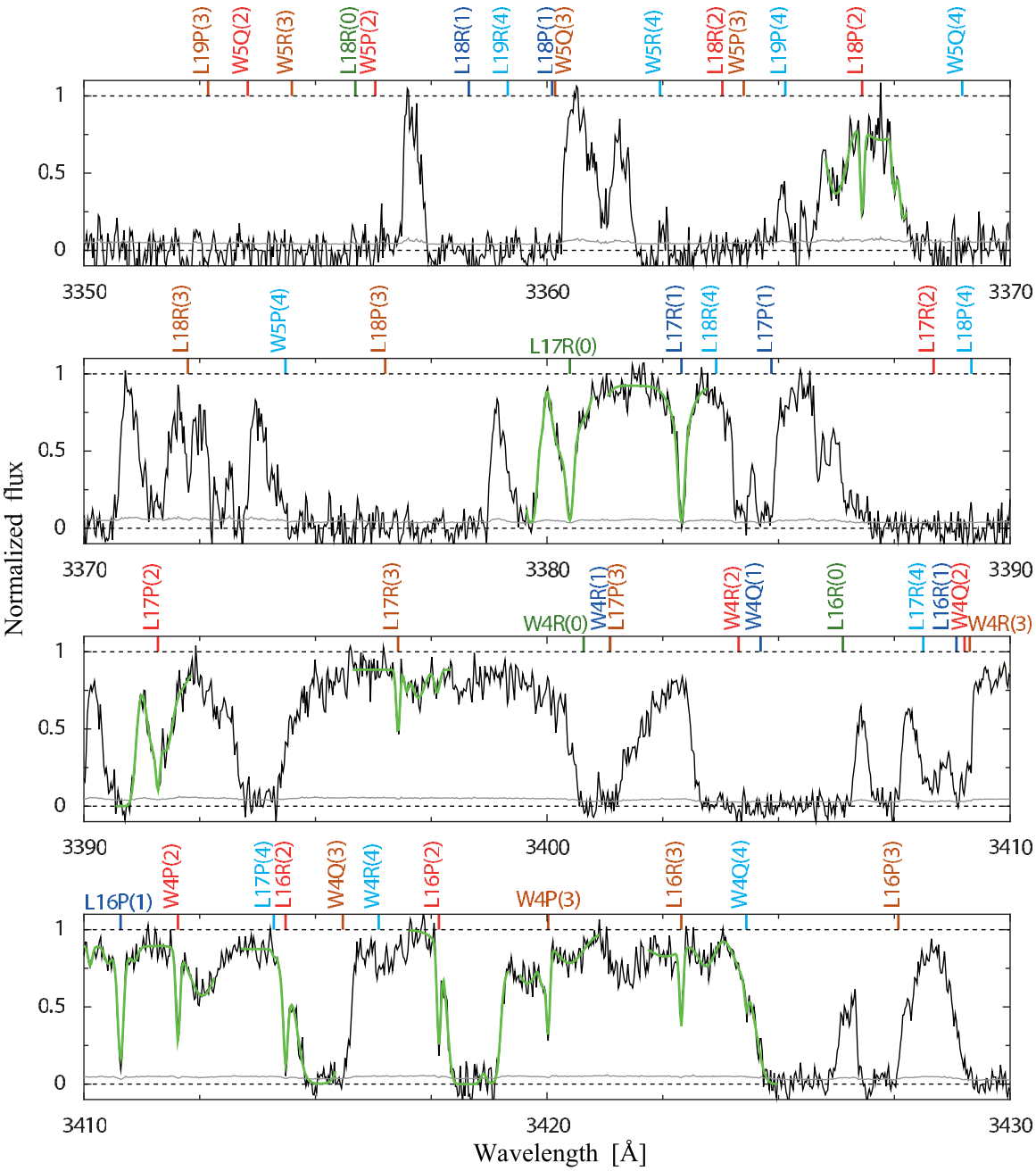

Figure 2. Part of the B0642−5038 spectrum with fitted H_2 absorptions. The tick marks are positioned at $z = 2.658603$. Different J transitions are labeled in different colors. The photons at the bluest wavelengths are cut out by the Lyman limit of the DLA.

(A color version of this figure is available in the online journal.)

Table 4

Column Densities, Doppler Widths, and Redshifts of the Fitted H_2 Transitions (Together with 1σ Statistical Uncertainties) as Reported by VPFIT

	1VC Model	2VC Model	
	$z = 2.6586026(4)$ $b = 1.57 \pm 0.04$ km s^{-1}	$z_1 = 2.6586030(4)$ $b_1 = 1.58 \pm 0.04$ km s^{-1}	$z_2 = 2.65851(12)$ $b_2 = 12.5 \pm 6.3$ km s^{-1}
J Level	log N (cm^{-2})	log N (cm^{-2})	log N (cm^{-2})
$J = 0$	18.15 ± 0.01	18.13 ± 0.02	13.97 ± 0.62
$J = 1$	18.20 ± 0.01	18.19 ± 0.01	13.74 ± 0.61
$J = 2$	16.21 ± 0.07	16.19 ± 0.07	...
$J = 3$	15.04 ± 0.05	15.03 ± 0.05	...
$J = 4$	13.72 ± 0.03	13.71 ± 0.03	...

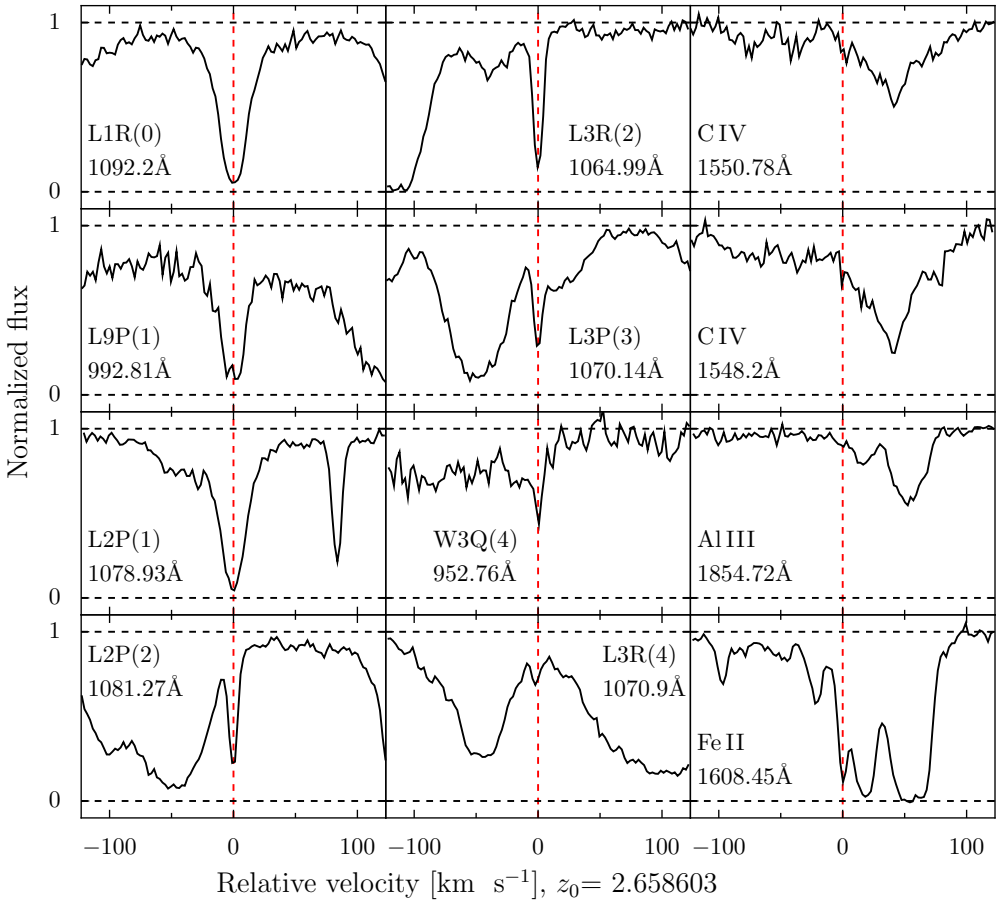

Figure 3. Some of the H_2 and metal transitions associated with the DLA at $z \sim 2.659$, displayed on a velocity scale. The red dashed line is centered at the redshift of the H_2 absorption. The C IV, Al III, and Fe II profiles show multiple absorption features spread over 200 km s^{-1}.
(A color version of this figure is available in the online journal.)

model as fiducial, but we perform further testing for robustness and consistency on both 1VC and 2VC models since the second VC is very weak.

Before proceeding with consistency tests focused on a μ-variation analysis, we use the measured column densities of H_2 to estimate some basic characteristics of the absorbing cloud. The column densities of different J transitions of H_2 provide a measure of the gas temperature in the cloud if the observed populations are in thermodynamic equilibrium and follow Boltzmann's law. The excitation temperature is defined with respect to the $J = 0$ level via $N_J/N_0 = g_J/g_0 \times e^{-E_{0J}/kT_{0J}}$. In Galactic diffuse clouds, the T_{01} temperature is regarded as a kinetic temperature of the gas (Roy et al. 2006). The higher levels are often populated in excess of the Boltzmann law, implying that besides collisions there are other processes involved, such as cascades following UV or formation pumping or, alternatively, shocks or turbulence effects (see, e.g., Cecchi-Pestellini et al. 2005). From the H_2 absorption in the DLA at $z = 2.659$ toward B0642−5038, we find a kinetic temperature of $T_{01} \simeq 84$ K, which is consistent with that in the Galactic interstellar medium (Rachford et al. 2002), while the levels at $J > 2$ indeed show higher temperatures of 100–140 K (see Figure 5). Both measured temperatures are consistent with what was found in other DLA studies (e.g., Srianand et al. 2005). Note that for the temperature calculations we used column densities from the 1VC model.

The total molecular column density amounts to $\log N(H_2) = 18.48 \pm 0.01$ cm^{-2}. Given the neutral content of $\log N(H\,I) = 20.95 \pm 0.08$ cm^{-2} (Noterdaeme et al. 2008), a molecular fraction of $\log f = -2.18 \pm 0.08$ is derived. Only 15% of DLAs with detected H_2 have a molecular fraction in the range $-4 < \log f < -1$ (Ledoux et al. 2003). For comparison, in the Galactic sightlines of similar neutral hydrogen density, typical values for the molecular hydrogen are $\log N(H_2) > 19$ (Rachford et al. 2002).

4.3. Consistency Tests

The results of the consistency tests discussed below are displayed in Figure 8. We start from a generic fit that includes all suitable transitions (111 in total) and data, i.e., all exposures independent of how they were calibrated (attached ThAr or not). Unless stated otherwise, in all the tests the z and b parameters are assumed to be the same for all J levels, and the column density N is the same for all transitions from a single J level for a single VC. The fitting solution is found through an iterative process, where at each iteration VPFIT checks the change in the relative χ^2 and stops when a stopping criterion is reached. We used a stopping criterion of $\Delta\chi^2/\chi^2 < 10^{-7}$ for a fine mode of fitting and $<10^{-6}$ for a coarse fitting. Whenever possible, we used the fine fitting mode, but in some cases this gave very slow convergence of the fit, and the coarse mode gave faster, more reliable results from a single minimization run of VPFIT. The 1VC generic model delivers $\Delta\mu/\mu = (16.9 \pm 4.4_{\rm stat}) \times 10^{-6}$, while the 2VC generic model results in $\Delta\mu/\mu = (17.1 \pm 4.5_{\rm stat}) \times 10^{-6}$; further tests

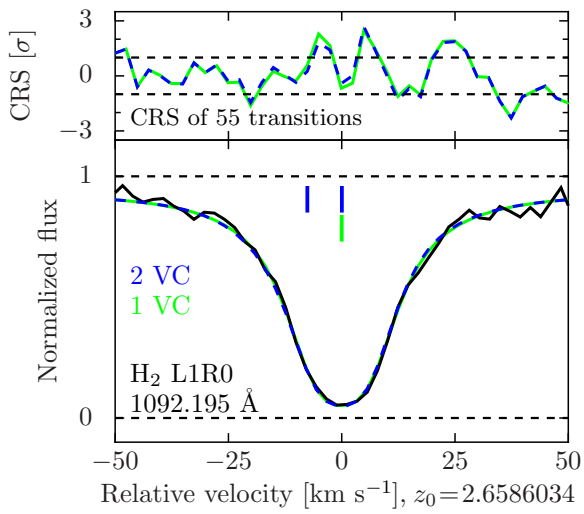

Figure 4. Composite residual spectrum (top) and an example of H_2 absorption centered at $z = 2.658603$. Fifty-five H_2 transitions were used to compose the composite residual spectrum. The black horizontal dashed lines in the composite residual plot show $\pm 1\sigma$ boundaries. The green line shows composite residuals (top) and a corresponding fit from the 1VC model and the blue line refers to the 2VC model.

(A color version of this figure is available in the online journal.)

and comparisons are made with respect to these results from generic tests.

In all the tests presented here, the transition oscillator strengths were kept fixed to the values established for the H_2 molecule. Note that the line intensities were derived in a model involving interactions between electronic states $B^1\Sigma_u^+$, $C^1\Pi_u$, $B'^1\Sigma_u^+$, and $D^1\Pi_u$ and intensity borrowing (Abgrall et al. 1994); no accurate transition oscillator strengths have been experimentally determined. In contrast, in previous analyses by Malec et al. (2010a) and King et al. (2011) for some specific transitions the oscillator strengths had to be adapted in the fitting procedure. In a study of three H_2 absorbing systems King et al. (2008) varied column densities (including a product with an oscillator strength) for each of the lines separately. In the present study we stuck as close as possible to the established molecular physics of H_2 and found no need to adapt oscillator strengths.

4.3.1. Isolating Low- and High-J Transitions

In this particular absorber, the $J = 0, 1$ and $J = 2$–4 transitions differ in that the former are saturated ($\log N > 18$ cm^{-2}; Table 4), unlike the latter. For this reason, if the velocity structure is underfitted (VCs missing), the lower-J level transitions would be affected more than the higher-J transitions because any missing components will be weak even in the low-J transitions and completely negligible in the high-J transitions. In other words, the low-J transitions can be more misleading when determining $\Delta\mu/\mu$ than the high-J transitions. For this reason, two more $\Delta\mu/\mu$ constraints are derived separately from the $J = 0, 1$ transitions (34 in total) and $J = 2$–4 transitions (77 in total) of the generic fit. Note that the tests are performed not by excluding unwanted transitions but by leaving their $\Delta\mu/\mu$ parameter fixed to zero. Constraints delivered from the $J = 0, 1$ transitions are $\Delta\mu/\mu = (7.9 \pm 6.2_{\rm stat}) \times 10^{-6}$ and $\Delta\mu/\mu = (18.7 \pm 7.2_{\rm stat}) \times 10^{-6}$ for the 1VC model and 2VC model, respectively. If only the $J = 2$–4 transitions are used, the 1VC and 2VC models deliver $\Delta\mu/\mu = (17.7 \pm 6.1_{\rm stat}) \times 10^{-6}$ and $\Delta\mu/\mu = (14.1 \pm 6.0_{\rm stat}) \times 10^{-6}$, respectively. As can be expected in the case of underfitting, the 1VC constraint from the $J = 0, 1$ transitions seems to be slightly off from the other constraints, including those from the generic fits.

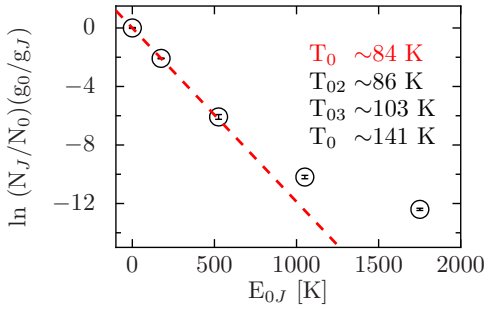

Figure 5. Excitation diagram for H_2 in the DLA at $z = 2.659$. The column densities are weighted with a factor $g_J = g_N(2J + 1)$, where g_N is the nuclear spin weight that has the value $g_N = 1$ for even values of J and $g_N = 3$ for odd values of J. The slope of a straight line gives $1/T_{01}$. The uncertainties of T_{0J}, as derived directly from measured column densities, are of the order of 3–5 K.

(A color version of this figure is available in the online journal.)

4.3.2. Separating Lyman and Werner Transitions

A test is performed where a $\Delta\mu/\mu$ constraint is delivered from either only Lyman band or only Werner band transitions. For the 1VC model we find $\Delta\mu/\mu = (15.5 \pm 4.5_{\rm stat}) \times 10^{-6}$ from the Lyman transitions and $\Delta\mu/\mu = (14.3 \pm 17.7_{\rm stat}) \times 10^{-6}$ from the Werner transitions. For the 2VC model it is, respectively, $\Delta\mu/\mu = (15.9 \pm 4.6_{\rm stat}) \times 10^{-6}$ and $\Delta\mu/\mu = (10.1 \pm 17.7_{\rm stat}) \times 10^{-6}$. The derived constraints are in good agreement with each other and with the generic fit results. However, the uncertainty of the constraints from Werner transitions is much larger than the one from Lyman transitions because there are around four times fewer Werner transitions in the fit. What the dominance of Lyman transitions over the fiducial result can imply is discussed in Section 5.5. Note again that the tests are performed not by excluding unwanted transitions but by leaving their $\Delta\mu/\mu$ parameter fixed to zero.

4.3.3. Excluding Problematic Regions

Seventeen H_2 transitions are blended with narrow lines, some of which are due to known metal absorbers, while others are unidentified. If the interloping lines are fitted inadequately, an effect in $\Delta\mu/\mu$ can be expected. To test this presumption, a fit without the regions containing these transitions is performed. For the 1VC and 2VC models the fitted subsample delivered, respectively, $\Delta\mu/\mu = (18.3 \pm 4.8_{\rm stat}) \times 10^{-6}$ and $\Delta\mu/\mu = (15.9 \pm 4.9_{\rm stat}) \times 10^{-6}$. The resulting constraints are in agreement with those from the generic fit which leads to a conclusion that contamination by metallic transitions does not affect positions of the H_2 transitions substantially.

4.3.4. Untying Free Parameters among Different J Levels

In the tests described above, redshifts and widths of the H_2 transitions were assumed to be the same, independent of J level. To test the validity of this assumption, the low- and high-J transitions are decoupled from each other and allowed to assume different z and b values to verify if the two groups deliver consistent constraints. One possibility why this may not be the case is a spatial inhomogeneity in temperature in the absorbing cloud. Also, by performing such a test we can test the possibility of an underfitted velocity structure as in Section 4.3.1. For the 1VC and 2VC models this test delivered, respectively, $\Delta\mu/\mu = (15.6 \pm 4.5_{\rm stat}) \times 10^{-6}$ and $\Delta\mu/\mu = (15.5 \pm 4.6_{\rm stat}) \times 10^{-6}$.

These constraints agree within uncertainties with those from the generic fits, which means that in the case of a relatively simple velocity structure of H_2, releasing some assumptions may not affect the $\Delta\mu/\mu$ considerably.

4.3.5. Fitting Parts of the Spectrum

In the presence of a long-range monotonic distortion of the wavelength scale, a significant effect on $\Delta\mu/\mu$ can potentially be generated, especially if only Lyman or only Werner transitions were fitted since the transitions in each band have monotonically increasing K_i coefficients toward the blue wavelengths. The degeneracy is possibly broken if both Lyman and Werner transitions are fitted in a common wavelength interval because, e.g., K_i (Werner) $= -0.01$, while K_i (Lyman) $= 0.03$ at 1010 Å (see Figure 1). On the other hand, the range where only Lyman transitions are present has a better S/N and therefore can have substantial weight in the comprehensive fit.

We separate and fit the part of the spectrum where both Lyman and Werner transitions are present, i.e., blueward from 3714 Å, and as a complementary test, we also fit the excluded Lyman transitions (redward from 3714 Å). For the 1VC test, the former test results in $\Delta\mu/\mu = (12.1 \pm 6.6_{\rm stat}) \times 10^{-6}$, and the latter results in $\Delta\mu/\mu = (15.4 \pm 9.9_{\rm stat}) \times 10^{-6}$. For the 2VC test, the results are $\Delta\mu/\mu = (11.1 \pm 6.7_{\rm stat}) \times 10^{-6}$ and $\Delta\mu/\mu = (17.9 \pm 10.0_{\rm stat}) \times 10^{-6}$, respectively. If the μ dependence of Werner transitions is removed, the fit (in the blue part) delivers $\Delta\mu/\mu = (10.5 \pm 6.7_{\rm stat}) \times 10^{-6}$ and $\Delta\mu/\mu = (9.7 \pm 6.8_{\rm stat}) \times 10^{-6}$ for the 1VC and 2VC models, respectively.

Generally, the constraints quoted above do not diverge significantly from those in the generic fit; however, there is a bias all of them can be affected by. In Section 4.3.2, it was demonstrated that the constraints derived from generic model are dominated by the Lyman transitions because of their disproportionate contribution to the data set. In the test where we disregard Lyman transitions in the red part (38 in total), the Lyman-to-Werner ratio is reduced to 2:1 compared to 4:1 in the generic fit. Thus, this approach should be less biased than the generic one, but it is still dominated by the Lyman transitions.

In Section 5.5 the possibility of long-range distortions is explored further.

5. SYSTEMATIC UNCERTAINTY

5.1. Calibration Residuals

One of the sources of systematic uncertainty is wavelength calibration residuals of ThAr lines. Typically, the residuals have a rms of 70 m s^{-1}; that is, at any given place in the spectrum the wavelength scale is accurate within 70 m s^{-1}. Usually, more than 10 ThAr lines are detected, and multiple H_2 transitions are fitted in each echelle order; therefore, the effect of any systematic trends is reduced to 30 m s^{-1} at most (Murphy et al. 2007). Given a span in K_i of 0.05, a velocity shift of 30 m s^{-1} translates into a $\Delta\mu/\mu$ shift of 2.0×10^{-6}, applying the following relation: $\Delta v = c\Delta K_i \Delta\mu/\mu$.

5.2. Nonattached ThAr

The UVES spectrograph is designed in such way that the grating is repositioned between different exposures. Although the repositioning of the grating should be accurate to within 0.1 pixel (D'Odorico et al. 2000), the ThAr calibrations can be obtained immediately after science observation, without initiating grating reset, so that potential uncertainties in the wavelength scale are avoided. The bulk of our exposures have attached ThAr calibrations (60% of the data). To test for possible miscalibration effects, we fit a "subspectrum," a spectrum comprising of only a subset of exposures but composed by the same process as the full spectrum, which includes only these "well-calibrated" exposures. For the S/N reduced from 35 to 32 at 370 nm, the 1VC model delivers $\Delta\mu/\mu = (16.7 \pm 4.9_{\rm stat}) \times 10^{-6}$, and the 2VC model delivers $\Delta\mu/\mu = (16.4 \pm 4.9_{\rm stat}) \times 10^{-6}$ (also see Figure 8). It can be concluded that the effect on $\Delta\mu/\mu$ due to data with nonattached ThAr is not evident in our case. However, this conclusion cannot be generalized and applied to every UVES spectrum; for example, in the case of varying α studies where just a few transitions are fitted in the spectrum, the effect, if present, might cause considerable shifts.

5.3. Intraorder Wavelength-scale Distortions

Whitmore et al. (2010) showed that intraorder distortions (i.e., distortions of the wavelength scale within echelle orders that repeat from order to order) up to ~100 m s^{-1} can be expected in VLT/UVES spectra. Thus, a ±100 m s^{-1} sawtooth wavelength distortion is introduced to each echelle order of the B0642−5038 spectrum using UVES_POPLER before they are combined into a single spectrum for analysis in VPFIT. Then, taking all 111 transitions into account, we perform a fit on a spectrum with the introduced intraorder wavelength-scale distortions. Results of such tests are model dependent, but generally, intraorder distortions are not expected to be a significant problem for μ-variation analysis because the H_2 transitions are spread over multiple orders. From the test that we performed on a distorted spectrum, we find a contribution to the systematic uncertainty of $\Delta\mu/\mu$ at the level of 0.6×10^{-6} (see Figure 8). The effect we find here is of the same order as in previous studies where such an analysis was also performed (Malec et al. 2010a; King et al. 2011; van Weerdenburg et al. 2011).

5.4. Uncertainty from Spectral Redispersion

To compose a final 1D spectrum, several echelle orders are combined by redispersing them onto a common wavelength scale and taking their weighted mean. The rebinning may cause flux correlations between neighboring pixels. Thus, the choice of a wavelength grid can, in principle, affect the measurement of $\Delta\mu/\mu$. To test this, we choose several slightly different grids in the range from 2.3 to 2.7 km s^{-1} per pixel. The maximal deviation among the resulting $\Delta\mu/\mu$ values is $\pm 3.0 \times 10^{-6}$. This is added to the total systematic uncertainty budget. Previous studies of different H_2 absorbers report deviations in $\Delta\mu/\mu$ due to redispersion in the range from 0.2×10^{-6} (van Weerdenburg et al. 2011) to 0.8×10^{-6} (Malec et al. 2010a) for pixel sizes ~1.3 km s^{-1} and to 1.4×10^{-6} (King et al. 2011) for ~2.5 km s^{-1} pixels, like those in the present analysis.

5.5. Long-range Wavelength-scale Distortions

The possibility of long-range distortions between the ThAr calibration spectra and quasar spectra recorded with VLT/UVES has been reported recently by Rahmani et al. (2013). In a study focusing on a μ-variation analysis from H_2 absorption toward HE0027–1836, Rahmani et al. (2013) report significant long-range calibration errors for UVES data, especially strong in exposures taken in 2012. Wavelength distortion errors, when using ThAr spectra for calibration, could, in principle, be produced by differing beam paths and/or slit illumination distributions between the quasar science exposure and the

subsequent ThAr calibration exposure. After reflecting from the primary, secondary, and tertiary mirrors, quasar light is directed through a derotator into the UVES enclosure. Once it enters the enclosure, the beam is split by a dichroic into the two arms of the spectrograph: a blue arm and a red arm. Each beam passes through its respective optics, which are a blue (red) slit, the cross dispersers, and several mirrors, and finally lands on the blue (red) CCD(s). The light from the calibration lamp is sent into the UVES enclosure by reflecting from a calibration mirror that is slid into the optical path of the telescope. After entering the enclosure, it interacts with the same optics described above. However, there could be an angular offset between the science and calibration exposures, which would result in slightly differing beam paths through the spectrometer, leading to a possible wavelength distortion. Also, each slit is illuminated fully by the ThAr lamp, while the quasars are unresolved point sources. Therefore, the quasar and ThAr light may produce different point-spread functions on the CCDs, and if that difference varies across the CCDs, a long-range distortion between the quasar and ThAr calibration may result.

Rahmani et al. (2013) used a cross-correlation technique to compare UVES spectra of various asteroids taken across several years with a solar spectrum recorded with a Fourier transform spectrometer (FTS). They found long-range velocity slopes, which they translated into systematic offsets for $\Delta\mu/\mu$ lying in the range between 2.5×10^{-6} and 13.3×10^{-6}. Prompted by the conclusions of Rahmani et al. (2013), we will later assess long-range wavelength distortions in the B0642−5038 spectrum using the asteroid method.

We first attempt to address the likely sign and magnitude of long-range distortions in the actual B0642−5038 spectra using simulations. In Section 4.3.5 we discussed the fact that the Werner and Lyman transitions, when fitted simultaneously, can break a possible degeneracy between long-range distortions and $\Delta\mu/\mu$. To illustrate this further, we use simulated spectra with distortions introduced following the formalism presented by Malec et al. (2010a, Section 4.2.2). The wavelength scale is compressed to simulate a long-range distortion, and the H_2 transitions are shifted to mimic a nonzero $(\Delta\mu/\mu)_{\rm sys}$. We used the 1VC generic model to produce simulated spectra with the same S/N as the real quasar spectrum, three different noise realizations in total. Each of these three simulated spectra was distorted to mimic $(\Delta\mu/\mu)_{\rm sys}$ of -17 and $+17 \times 10^{-6}$ and fitted using the 1VC generic model including all 111 H_2 transitions. As expected, the $\Delta\mu/\mu$ values returned from fitting agree with $(\Delta\mu/\mu)_{\rm sys}$ within uncertainties; they also agree within uncertainties when the undistorted simulations (i.e., $(\Delta\mu/\mu)_{\rm sys} = 0$) were analyzed. In other words, in the relationship $\Delta\mu/\mu = s_1 \times (\Delta\mu/\mu)_{\rm sys} + b_1$, the coefficient s_1 is close to unity and b_1 is of the order of $\Delta\mu/\mu$ statistical uncertainty.

In a second step, the same simulated spectra with long-range distortions were used to derive $\Delta\mu/\mu$ constraints separately from the blue and red parts (with a dividing line at 3714 Å as in Section 4.3.5). To compare the constraints returned from the blue part with those from the red part, we use the relationship $(\Delta\mu/\mu)_{\rm red} - (\Delta\mu/\mu)_{\rm blue} = s_2 \times (\Delta\mu/\mu)_{\rm sys} + b_2$. In this case, an s_2 coefficient close to unity means that the blue part is very resistant to the long-range distortions represented by $(\Delta\mu/\mu)_{\rm sys}$. From our simulated spectra we derive $s_2 \simeq 0.8$. The real quasar spectrum fitted with a 1VC model returns $(\Delta\mu/\mu)_{\rm red} - (\Delta\mu/\mu)_{\rm blue} = (3.3 \pm 11.9) \times 10^{-6}$ (see Section 4.3.5). Assuming b_2 is negligible (a few 10^{-6}), we can estimate the size of a possible linear wavelength distortion in the real spectrum: $(\Delta\mu/\mu)_{\rm sys} = (3.3 \pm 11.9) \times 10^{-6}/0.8 = (4 \pm 15) \times 10^{-6}$. The possible distortion itself is not large, but it has a large uncertainty, which makes the interpretation difficult.

A different way of quantifying long-range distortions is to observe objects with a well-understood spectrum that can then be compared with a reference spectrum. An iodine cell has been used to quantify the calibration differences between the ThAr wavelength solution of quasar spectra observed with the iodine cell in the line of sight and a reference FTS iodine cell spectrum (Griest et al. 2010; Whitmore et al. 2010). We use a new implementation of this "supercalibration" method (J. B. Whitmore et al., in preparation), which is similar to the iodine cell. The only practical difference is instead of using the iodine cell spectrum as a reference, we use the solar spectrum. The general procedure for finding a velocity shift $v_{\rm shift}$ between the ThAr solution and the FTS reference spectrum begins by using a science exposure that has been calibrated in the standard way that our a quasar exposures were calibrated: (1) take a science exposure, (2) take a ThAr calibration exposure, and (3) solve for the ThAr wavelength solution. After these steps are completed, the supercalibration technique solves for relative velocity shifts between the science exposure's ThAr wavelength solution and a reference spectrum.

The details of how we implement this supercalibration technique for this paper are as follows. We use the FTS solar spectrum KPNO2010 detailed in Chance & Kurucz (2010), which is publicly available,[7] as our reference spectrum. We chose an archival exposure of the asteroid Ceres taken in 2007 December, a few days before the beginning of the quasar observations (which span the next 2 months; see Table 1). Also, we used a number of the solar twin HD 28099 and HD 76151 spectra observed a month later than Ceres, conveniently close in time to the bulk of the quasar observations (see Figure 7). A 500 km s^{-1} segment of the spectrum is taken from the asteroid/solar twin science exposure, and an overlapping region of the solar FTS spectrum is taken as the model. The model is modified by the following five-parameter transformation: (1) a single velocity shift, (2) a multiplicative flux scaling factor, (3) an additive flux offset factor, (4) the sigma width of a symmetric Gaussian instrument profile, and (5) a linear continuum slope correction. We minimize χ^2 between the model and the data. The wavelength ThAr corrections found with this supercalibration technique are reported as $v_{\rm shift}$ with the following sign conventions:

$$\lambda_{\rm shift} = \lambda_{\rm reference} - \lambda_{\rm ThAr}, \quad (4)$$

$$v_{\rm shift} = c \times \frac{\lambda_{\rm shift}}{\lambda}. \quad (5)$$

The supercalibration technique is sensitive to both short- and long-range distortions. Since the contribution to the systematic error budget of short-range (intraorder) distortions is quantified in Section 5.3, the long-range distortions remain to be incorporated. A plot of the average $v_{\rm shift}$ per order, with an error bar that is the size of the standard deviations, is shown in Figure 6. We fit a linear model of the long-range distortion and use this model in our analysis.

As can be seen from Figure 7(a), a correction derived from the Ceres observations is twice as big as the one from the solar twins. We apply these two corrections to the spectrum

[7] http://kurucz.harvard.edu/sun/irradiance2005/irradthu.dat

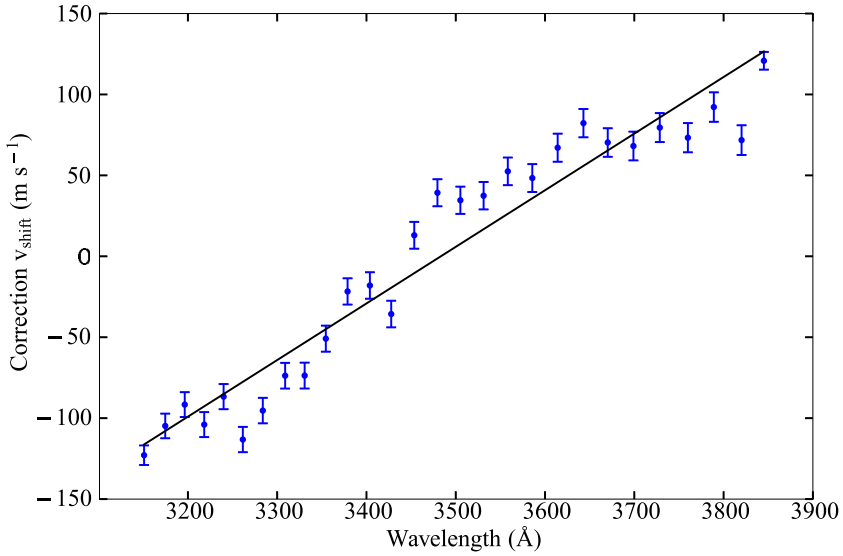

Figure 6. Plot of the long-range wavelength distortion found by the supercalibration technique in the Ceres 2007 exposure (orders 5–33). The $v_{\rm shift}$, as defined in Equation (5), is the correction that needs to be applied to the ThAr wavelength solution to align with the fiducial FTS solar spectrum. We plot the average $v_{\rm shift}$ for each echelle order, and the size of the error bar is the standard deviation of the $v_{\rm shift}$ within that order. The plot has been shifted by a constant velocity to account for radial velocity and slit-offset effects. In other words, the absolute scale is not meaningful, but the relative scale is informative. The equation of the best fit line is $v_{\rm shift}(\lambda) = A \times \lambda + B$, with $A = 350$ m s^{-1} per 1000 Å and $B = -1218.0$ m s^{-1}.

(A color version of this figure is available in the online journal.)

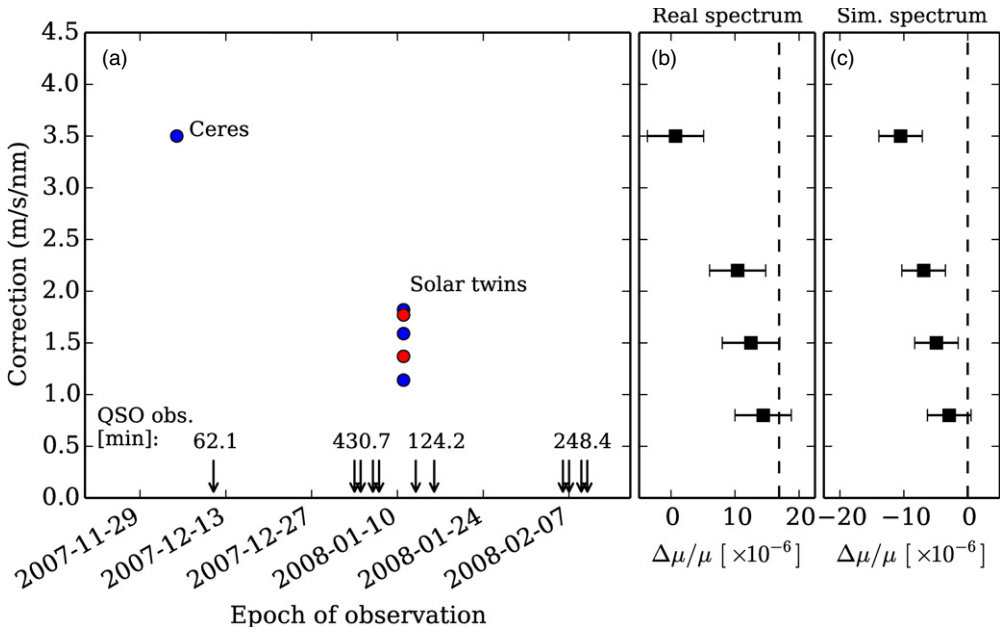

Figure 7. (a) Corrections of the wavelength scale, as derived from observations of Ceres and solar twins, are displayed vs. the observing epoch. Blue (red) points refer to corrections of the wavelengths at <450 nm (>450 nm). Quasar observations from program 080.A-0288(A) are marked on the time axis; most of them were conducted around the time when the solar twin spectra were taken. (b) The data points refer to the $\Delta\mu/\mu$ constraints as derived from the B0642−5038 spectrum when wavelength corrections are applied to it (1VC model). The vertical dashed line shows a $\Delta\mu/\mu$ constraint from an uncorrected spectrum. Applying wavelength corrections results in $\Delta\mu/\mu$ values that deviate from zero less than the one from the uncorrected spectrum. Note that we apply wavelength corrections to the total averaged spectrum and not to the individual exposures. (c) A simulated quasar spectrum is skewed using the same wavelength corrections as in panel (b). Corrections of this sign result in a $\Delta\mu/\mu$ measurement smaller than the input $\Delta\mu/\mu = 0$ (indicated by the dashed vertical line). A correction of 3.5 m s^{-1} nm^{-1} (implied by Ceres observations) leads to a $\Delta\mu/\mu$ shift from 0 to -10.5×10^{-6}. A correction based on the solar twin (1.5 m s^{-1} nm^{-1}) results in a $\Delta\mu/\mu$ shift from 0 to -4.9×10^{-6}. The uncertainties of the $\Delta\mu/\mu$ constraints are defined by the S/N of the simulated spectrum.

(A color version of this figure is available in the online journal.)

of B0642−5038 (1VC model) and derive, respectively, $\Delta\mu/\mu$ of $(0.7 \pm 4.4_{\rm stat}) \times 10^{-6}$ and $(12.5 \pm 4.4_{\rm stat}) \times 10^{-6}$. These values, especially the former, differ substantially from an uncorrected measurement ($\Delta\mu/\mu = (16.9 \pm 4.4_{\rm stat}) \times 10^{-6}$). As an additional test, we apply the corrections to a simulated spectrum. Similar to what we did before, we used the 1VC generic model to produce a simulated spectrum with the same S/N as the real quasar spectrum and imposed $\Delta\mu/\mu = 0$. Fitting this spectrum with two different correction values results in $\Delta\mu/\mu$ of $(-10.5 \pm 3.4_{\rm stat}) \times 10^{-6}$ (larger correction from Ceres) and $(-4.9 \pm 3.4_{\rm stat}) \times 10^{-6}$ (smaller correction from the solar twins). In both cases, when the corrections are applied to

the real and simulated spectrum, the measured $\Delta\mu/\mu$ value is smaller than that from a corresponding uncorrected spectrum (see Figures 7(b) and (c)). In other words, if the long-range wavelength distortions are neglected, the measured $\Delta\mu/\mu$ will likely be more positive than its actual value. A number of asteroid calibrations taken with UVES over surrounding years agree on the sign of the effect. These offsets are relatively large, exceeding the estimates of statistical uncertainties and other systematic effects (Rahmani et al. 2013). However, an important question to be addressed when making a correction to $\Delta\mu/\mu$ is that of the accuracy of the correction. As can be seen from Figure 7(a), most of the quasar exposures are taken within ± 8 days of the observations of the solar twins, and thus, we further rely on the solar twins in making an adjustment of the fiducial $\Delta\mu/\mu$ measurement; that is, we use $\Delta\mu/\mu = -4.4 \times 10^{-6}$ as a correction. Note also that the same central wavelengths (setting of the dichroic) have been adopted in the observations of the solar twins and quasar, although that is not the case for the Ceres asteroid (see Table 1). Nevertheless, we include the latter measurement in the estimation of the $\Delta\mu/\mu$ correction accuracy, which we base on a spread in the derived wavelength correction values over a month's time (Figure 7(a)). A standard deviation of the averaged correction values equals ± 0.7 m s^{-1} nm^{-1}, and thus, we fit spectra corrected by ± 0.7 m s^{-1} nm^{-1} with respect to the correction from the solar twins (1.5 m s^{-1} nm^{-1}). These corrections result in $\Delta\mu/\mu$ shifts of $\pm 2.0 \times 10^{-6}$ with respect to the results derived from both the real quasar spectrum and the simulated spectrum. Thus, we further add $\pm 2.0 \times 10^{-6}$ to the systematic error budget of $\Delta\mu/\mu$.

5.6. Summary of Systematic Uncertainty

From the performed tests we estimate four definite contributions to the total systematic error of $\Delta\mu/\mu$: the calibration residuals can contribute up to 2.0×10^{-6}, the intraorder distortions can introduce an error of 0.6×10^{-6}, an effect of 0.7×10^{-6} can be expected due to nonattached ThAr calibrations, and the spectral redispersion may introduce an error of 3.0×10^{-6}. Adding these four contributions in quadrature, we obtain the total systematic error of $\Delta\mu/\mu = 3.7 \times 10^{-6}$. The resulting constraint is then $\Delta\mu/\mu = (17.1 \pm 4.5_{\rm stat} \pm 3.7_{\rm sys}) \times 10^{-6}$. Analysis of solar twin and asteroid spectra shows that an additional systematic effect pertaining to wavelength miscalibration over long ranges is found in the quasar spectrum. Due to this miscalibration the $\Delta\mu/\mu$ measurement may have been shifted toward more positive values. Although both the asteroid and solar twin calibrations suggest corrections of the same sign, their magnitudes differ by a factor of two. In making a correction, we rely on the solar twin spectra, which are taken closer in time to most of the quasar observations and with the same spectrograph settings. They deliver a $\Delta\mu/\mu$ correction of $(-4.4 \pm 2.0_{\rm sys}) \times 10^{-6}$ and hence a corrected $\Delta\mu/\mu$ of $(12.7 \pm 4.5_{\rm stat} \pm 4.2_{\rm sys}) \times 10^{-6}$.

6. DISCUSSION

In the present study ESO archival spectra toward a quasar system B0642−5038 with a DLA at redshift 2.659 are analyzed to extract information on a possible variation of the proton–electron mass ratio μ. The DLA contains a molecular fraction of $\log f = -2.18 \pm 0.08$ in which 111 H_2 lines were identified as usable for a μ-variation analysis. The spectrum is of good quality and has a S/N of ∼35 in the relevant wavelength region of H_2 absorbers, which is just a bit lower than some other systems that were analyzed previously, e.g., J2123−0050 (Malec et al. 2010a; van Weerdenburg et al. 2011), Q0528−250 (King et al. 2008, 2011), Q0405−443 (King et al. 2008), and Q0347−383 (King et al. 2008; Wendt & Molaro 2012), and better than Q2348−011 (Bagdonaite et al. 2012) and HE0027−1836 (Rahmani et al. 2013).

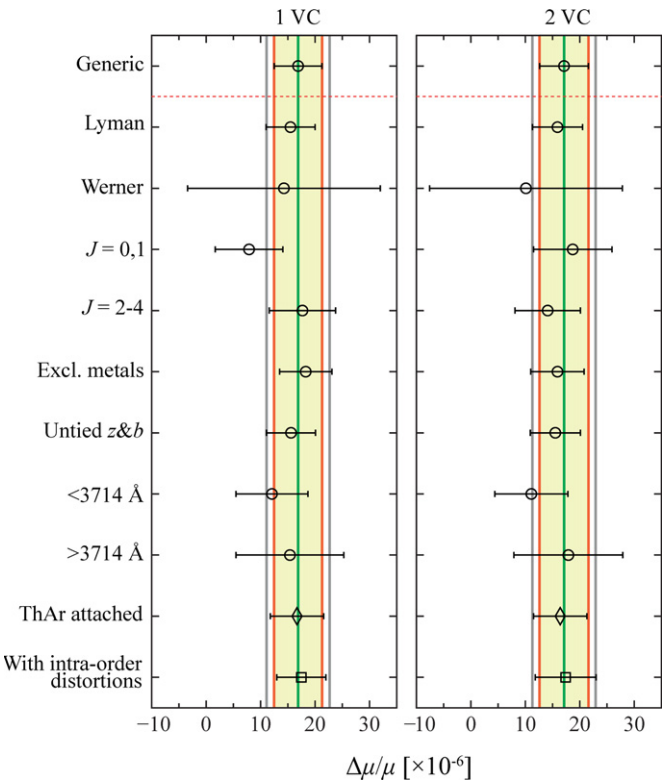

Figure 8. Constraints from various tests described in Section 4.3 are displayed for comparison with the one from a generic model that includes all 111 transitions and all available spectral data. The vertical green line in each panel indicates the $\Delta\mu/\mu$ value from the generic test. The shaded area and red (gray) vertical lines indicate the 1σ statistical (statistical and systematic) uncertainties associated with the constraints from the generic tests. The two bottom constraints are used to estimate systematic error on $\Delta\mu/\mu$ due to potential wavelength-scale inaccuracies described in Sections 5.1–5.4.

(A color version of this figure is available in the online journal.)

The resulting value of $\Delta\mu/\mu = (17.1 \pm 4.5_{\rm stat} \pm 3.7_{\rm sys}) \times 10^{-6}$ represents a result that is in itself a remarkable 3σ effect on a varying constant. However, we find evidence for a long-range distortion of the wavelength scale in the analyzed spectrum. On the basis of our analysis of asteroid and solar twin spectra and on a similar study by Rahmani et al. (2013) we conclude that because of long-range distortions $\Delta\mu/\mu$ in this spectrum has shifted away from its actual value toward more positive values. Although the sign of this systematic error seems to be consistent among data taken in different epochs, the amplitude appears to be varying. We use solar twin spectra that are taken close in time to the quasar observations to make a correction that reduces the significance of the initial measurement and delivers $\Delta\mu/\mu = (12.7 \pm 4.5_{\rm stat} \pm 4.2_{\rm sys}) \times 10^{-6}$ or $(12.7 \pm 6.2) \times 10^{-6}$ if the uncertainties are added in quadrature.

Regarding the analysis presented here, of great importance is the consistency found in the statistical and systematic tests performed on the data set. These tests, results of which are graphically displayed in Figure 8, constitute VC analysis, the separate effect of subsets of Lyman and Werner bands, separate sets of populated rotational states associated with

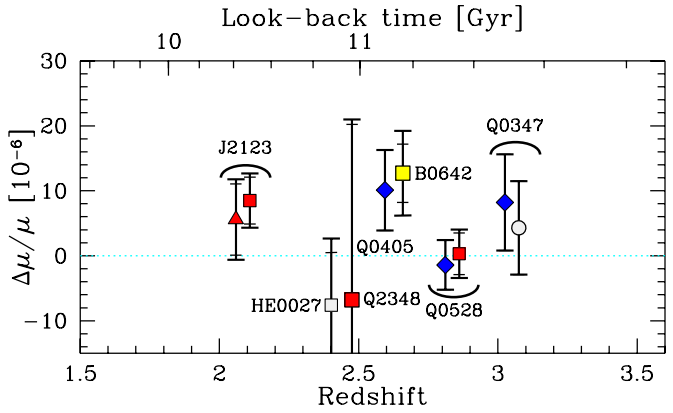

Figure 9. $\Delta\mu/\mu$ constraints from H_2 in seven different quasar sightlines: Q0528−250 (King et al. 2008, 2011), J2123−0050 (Malec et al. 2010a; van Weerdenburg et al. 2011), Q0347−383 (King et al. 2008; Wendt & Molaro 2012), Q2348−011 (Bagdonaite et al. 2012), Q0405−443 (King et al. 2008), HE0027−1836 (Rahmani et al. 2013), and B0642−5038 (this work). Note that some absorbers where analyzed more than once; in these cases one of the points is offset on the z scale by +0.05 to avoid overlap. Also, the Q2348 point is offset by +0.05 to avoid overlap with HE0027, which is located at a similar redshift. All the constraints shown here are derived by employing the comprehensive fitting method, except for a constraint from Q0347−383, shown as a gray circle (Wendt & Molaro 2012).

(A color version of this figure is available in the online journal.)

cold and warm molecular fractions, separation of wavelength regions, and effects of short-range (i.e., intraorder) distortions of the wavelength scale. No significant difference was found between the sets of quasar exposures with attached ThAr calibration spectra and the sets for which the ThAr calibration was performed at the end of the night after resets of the grating in the spectrometer.

The presented $\Delta\mu/\mu$ constraint can be viewed in the perspective of the entire set of results that is currently being produced for H_2 absorptions at high redshift. In Figure 9 this data set is plotted. From all the analyses being performed we have collected those results that were obtained through the comprehensive fitting method. In previous reports an extensive discussion is provided on the advantages of the comprehensive fitting over the line-by-line method (Malec et al. 2010a; King et al. 2008). Only for the case where a single VC is definitive, such as in Q0347−383 (Wendt & Molaro 2012), is a result from a line-by-line analysis included in the overview. Averaging over the presented data set results in $\Delta\mu/\mu = (4.0 \pm 1.8) \times 10^{-6}$ for look-back times in the range of 10–12 billion years.

Naturally, a question arises as to what extent the $\Delta\mu/\mu$ constraints measured in the past are affected by the long-range wavelength miscalibration. In the data set displayed in Figure 9, only the constraints from the B0642−5038 and HE0027−1836 quasar sight lines are derived with the long-range wavelength distortion effect taken into account. According to the present study, wavelength distortions can vary in amplitude within one night as well as over a month's time, while Rahmani et al. (2013) found year-to-year changes. Thus, regarding the H_2 absorbers that have been analyzed so far, a case-by-case reanalysis might be necessary, where this newly found systematic effect is investigated. Although from the currently available information it seems likely that the individual and average $\Delta\mu/\mu$ measurements are biased toward more positive values, the two examples discussed further reinforce the motivation for individual reanalysis using absolute calibration methods such as the supercalibration method. As for VLT/UVES, a detailed and very accurate study was made for the Q0528−250 H_2 absorbing system. On the basis of UVES data recorded in 2003 January reported by Ivanchik et al. (2005), King et al. (2008) performed a reanalysis with the comprehensive fitting method and retrieved a constraint of $\Delta\mu/\mu = (-1.4 \pm 3.9) \times 10^{-6}$. On the basis of an independent data set for Q0528−250, recorded in the period 2008 November to 2009 February, King et al. (2008) deduced a constraint of $\Delta\mu/\mu = (0.3 \pm 3.7) \times 10^{-6}$, in perfect agreement, while the data sets of the same object analyzed by the same methods were obtained over a time interval of 6 yr. Because it is not understood how the long-range wavelength distortions change with time, it remains to be seen whether it is just a coincidence that these two constraints were affected similarly. Further, there is a result on the analysis of H_2 absorption toward J2123−0050 from two different telescopes. While Malec et al. (2010a) obtained $\Delta\mu/\mu = (5.6 \pm 5.6_{\rm stat} \pm 2.9_{\rm sys}) \times 10^{-6}$ from an observation of J2123−0050 with HIRES/Keck, van Weerdenburg et al. (2011) obtained $\Delta\mu/\mu = (8.5 \pm 3.6_{\rm stat} \pm 2.2_{\rm sys}) \times 10^{-6}$ from VLT/UVES, also in good agreement. Here it is noted that the same comprehensive fitting method was used in both analyses and that, so far, J2123−0050 is the best H_2 absorbing system analyzed in terms of brightness of the background quasar and the column density of the H_2 absorbing galaxy. This particular absorber was investigated in a recent study by Evans & Murphy (2013), in which direct comparison of the HIRES/Keck and VLT/UVES spectra was made to detect possible relative velocity shifts between the two. Although some indications of a constant offset between the spectra were found, no significant wavelength-dependent shift could be detected. The sensitivity of the direct comparison method is similar to that of the supercalibration approach used in the current study (a few m s^{-1} nm^{-1}). Thus, the results by Evans & Murphy (2013) might be held as counterevidence against long-range distortions of the UVES wavelength calibration, unless HIRES/Keck suffers from a similar problem. More investigations of this phenomenon are urgently needed, in particular for studies such as the present one that require understanding of the calibration of the spectrometer at its extreme limits. This would lead to establishing a firm constraint on a variation of μ at redshifts $z \sim 2$–3.

Studies at lower redshifts, based on the ammonia and methanol methods, yield a constraint of μ varying at the level of less than 3×10^{-7} (Henkel et al. 2009; Kanekar 2011; Bagdonaite et al. 2013a, 2013b). These strongly constraining findings, produced from absorbing clouds toward PKS1830−211 and B0218+357, may be interpreted as contradictive to less constraining results beyond $z > 2$. In view of physical models linking coupling strengths to the ratio of matter versus dark energy in the universe, where variation of constants is frozen by dark energy (Sandvik et al. 2002; Barrow et al. 2002), it remains important to search for drifting constants in various evolutionary stages of the universe, i.e., at different redshifts.

This work was financially supported by the Netherlands Foundation for Fundamental Research (FOM). W.U. acknowledges funding from the Templeton foundation. M.T.M. and J.B.W. thank the Australian Research Council for Discovery Project grant DP110100866 which supported this work.

Note added in proof. During the review process of the present work, a paper was published describing an analysis of the same ESO-archive data set on the QSO B0642−5038

object analyzed here. The study by Albornoz Vásquez et al. (2014), submitted on 26 August 2013, reports a constraint of $\Delta\mu/\mu = (7.4 \pm 4.3_{\rm stat} \pm 5.1_{\rm sys}) \times 10^{-6}$. However, they did not take into account the long-range wavelength distortions considered in the present study.

Facilities: VLT:Kueyen (UVES)

REFERENCES

Abgrall, H., Roueff, E., Launay, F., & Roncin, J.-Y. 1994, CaJPh, 72, 856
Akaike, A. 1974, ITAC, 19, 716
Albornoz Vásquez, D., Rahmani, H., Noterdaeme, P., et al. 2014, A&A, in press
Bagdonaite, J., Daprà, M., Jansen, P., et al. 2013a, PhRvL, 111, 231101
Bagdonaite, J., Jansen, P., Henkel, C., et al. 2013b, Sci, 339, 46
Bagdonaite, J., Murphy, M. T., Kaper, L., & Ubachs, W. 2012, MNRAS, 421, 419
Barrow, J. D., Sandvik, H. B., & Magueijo, J. 2002, PhRvD, 65, 123501
Bekenstein, J. D. 2002, PhRvD, 66, 123514
Cecchi-Pestellini, C., Casu, S., & Dalgarno, A. 2005, MNRAS, 364, 1309
Chance, K., & Kurucz, R. L. 2010, JQSRT, 111, 1289
D'Odorico, S., Cristiani, S., Dekker, H., et al. 2000, Proc. SPIE, 4005, 121
Edlén, B. 1966, Metro, 2, 71
Evans, T. M., & Murphy, M. T. 2013, ApJ, 778, 173
Flambaum, V. V., & Kozlov, M. G. 2007, PhRvL, 98, 240801
Flambaum, V. V., Leinweber, D. B., Thomas, A. W., & Young, R. D. 2004, PhRvD, 69, 115006
Griest, K., Whitmore, J. B., Wolfe, A. M., et al. 2010, ApJ, 708, 158
Henkel, C., Menten, K. M., Murphy, M. T., et al. 2009, A&A, 500, 725
Ivanchik, A., Petitjean, P., Varshalovich, D., et al. 2005, A&A, 440, 45
Ivanov, T. I., Roudjane, M., Vieitez, M. O., et al. 2008, PhRvL, 100, 093007
Jansen, P., Xu, L.-H., Kleiner, I., Ubachs, W., & Bethlem, H. L. 2011, PhRvL, 106, 100801
Kanekar, N. 2011, ApJL, 728, L12
King, J. A. 2012, PhD thesis, UNSW
King, J. A., Murphy, M. T., Ubachs, W., & Webb, J. K. 2011, MNRAS, 417, 3010
King, J. A., Webb, J. K., Murphy, M. T., & Carswell, R. F. 2008, PhRvL, 101, 251304
King, J. A., Webb, J. K., Murphy, M. T., et al. 2012, MNRAS, 422, 3370
Ledoux, C., Petitjean, P., & Srianand, R. 2003, MNRAS, 346, 209
Levshakov, S. A., Kozlov, M. G., & Reimers, D. 2011, ApJ, 738, 26
Malec, A. L., Buning, R., Murphy, M. T., et al. 2010a, MNRAS, 403, 1541
Malec, A. L., Buning, R., Murphy, M. T., et al. 2010b, yCat, 740, 31541
Meshkov, V. V., Stolyarov, A. V., Ivanchik, A., & Varshalovich, D. A. 2006, JETPL, 83, 303
Murphy, M. T., Flambaum, V. V., Muller, S., & Henkel, C. 2008a, Sci, 320, 1611
Murphy, M. T., Tzanavaris, P., Webb, J. K., & Lovis, C. 2007, MNRAS, 378, 221
Murphy, M. T., Webb, J. K., & Flambaum, V. V. 2008b, MNRAS, 384, 1053
Noterdaeme, P., Ledoux, C., Petitjean, P., & Srianand, R. 2008, A&A, 481, 327
Rachford, B. L., Snow, T. P., Tumlinson, J., et al. 2002, ApJ, 577, 221
Rahmani, H., Wendt, M., Srianand, R., et al. 2013, MNRAS, 435, 861
Reinhold, E., Buning, R., Hollenstein, U., et al. 2006, PhRvL, 96, 151101
Roy, N., Chengalur, J. N., & Srianand, R. 2006, MNRAS, 365, L1
Salumbides, E. J., Dickenson, G. D., Ivanov, T. I., & Ubachs, W. 2011, PhRvL, 107, 043005
Salumbides, E. J., Niu, M. L., Bagdonaite, J., et al. 2012, PhRvA, 86, 022510
Sandvik, H. B., Barrow, J. D., & Magueijo, J. 2002, PhRvL, 88, 031302
Srianand, R., Petitjean, P., Ledoux, C., Ferland, G., & Shaw, G. 2005, MNRAS, 362, 549
Thompson, R. I. 1975, ApL, 16, 3
Ubachs, W., Bagdonaite, J., Murphy, M. T., Buning, R., & Kaper, L. 2011, in Astrophysics and Space Science Proceedings, From Varying Couplings to Fundamental Physics, ed. C. Martins & P. Molaro (Berlin: Springer), 125
Ubachs, W., Buning, R., Eikema, K. S. E., & Reinhold, E. 2007, JMoSp, 241, 155
Uzan, J.-P. 2011, LRR, 14, 2
van Weerdenburg, F., Murphy, M. T., Malec, A. L., Kaper, L., & Ubachs, W. 2011, PhRvL, 106, 180802
Webb, J. K., King, J. A., Murphy, M. T., et al. 2011, PhRvL, 107, 191101
Wendt, M., & Molaro, P. 2012, A&A, 541, A69
Whitmore, J. B., Murphy, M. T., & Griest, K. 2010, ApJ, 723, 89